Supporting Information

Fabrication and Properties of a Free-Standing Two-Dimensional Titania

Song Ling Wang,[†,#] Xin Luo,[‡,§,#] Xiong Zhou,[∥] Ye Zhu,[§] Xiao Chi,[⊥] Wei Chen,[†] Kai Wu,[∥] Zheng Liu,[▲] Su Ying Quek,*[,‡,⊥] Guo Qin Xu*[,†]

[†]Department of Chemistry, National University of Singapore, 3 Science Drive 3, Singapore 117543, Singapore

[‡]Centre for Advanced 2D Materials, National University of Singapore, 6 Science Drive 2, Singapore 117546, Singapore

[§]Department of Applied Physics, The Hong Kong Polytechnic University, Hung Hom, Kowloon, Hong Kong, P. R. China

[∥]College of Chemistry and Molecular Engineering, Peking University, Beijing 100871, P. R. China

[⊥]Department of Physics, National University of Singapore, 2 Science Drive 3, Singapore 117551, Singapore

[▲]School of Materials Science and Engineering, Nanyang Technological University, 50 Nanyang Avenue, Singapore 639798, Singapore

Experimental and Theoretical Sections

1. Synthesis of free-standing 2-D TiO_2. 1.00 mL of Titanium (IV) butoxide was added into oleylamine (5.00 mL) under magnetic stirring at room temperature. After stirring around 10 min, the red color could be immediately seen when the 5.00 mL of 1,2-ethanedithiol was dropped into the above mixed solution. The resulting precursor was stirred and subsequently transferred to a 50 mL autoclave for solvothermal reaction at 200 ^{o}C for 24 h. Upon completion, the autoclave was cooled down to room temperature. We first washed the obtained sample using ethanol for several times. Then the 1:6 volume ratio of hexane or toluene:ethanol was used to further wash the as-prepared sample. Finally, the free-standing 2-D TiO_2 material was collected after freeze-drying in a vacuum chamber, followed by drying in air at 60 ^{o}C.

2. Photocurrent densities measurement. A three-electrode system was used to measure the photocurrent signals. The working electrode is the synthesized 2-D TiO_2 sample coated on ITO (1 cm × 0.5 cm). Platinum gauze and Ag/AgCl served as the counter and reference electrodes, respectively. The NaOH aqueous solution (1.00 M) was the electrolyte in a quartz reaction cell. A 500 W xenon lamp provided the simulated sunlight. Light with a specific wavelength was obtained by mounting an appropriate filter on the 500 W xenon lamp. The light transmittance ratios of filters used have also been identified by optical spectroscopy (Figure S12). The chronoamperometric measurement of 2-D TiO_2 material was obtained at 0.00 V while the simulator was switched on and off every 10 seconds manually using a shutter to record the change in photocurrent signals. We tested photocurrent densities of the 2-D TiO_2 material under light irradiation with various wavelengths, including 450, 475, 500, 550, 600, 700, and 800 nm.

3. Degradation of rhodamine B (RhB). 15.0 mg of 2-D TiO_2 was added into RhB aqueous solution (15.0 ml, 20.0 mg/L) followed by ultrasonication for around 5 min. Under magnetic stirring, this solution was kept in darkness for 1 hour at room temperature to reach the adsorption-desorption equilibrium. A 500 W xenon lamp fixed with filter (400 nm) was used as the light source. 3.0 mL of the reactive solution was sampled after light irradiation for four hours. The supernatant solution with RhB molecules was obtained by centrifuging and removing the 2-D TiO_2 catalyst precipitate. Thus, the concentration of the remaining RhB molecules was measured by using UV-vis absorption spectrophotometer. Following this procedure, degradation of RhB was also conducted at other wavelengths (500, 600, 700, and 800 nm). For comparison, we also tested the degradations of RhB over the bulk TiO_2 (Degussa P25) with the same experimental procedure.

4. Detection of singlet oxygen ($^1O_2$) generation. The generation of singlet $^1O_2$ species under light excitation was monitored by chemical oxidation of 9, 10-anthracenediyl-bis (methylene) dimalonic acid (ABDA) molecules. Note that ABDA reacts irreversibly with $^1O_2$, leading to the decrease in the absorption of ABDA. The aqueous solution prepared by mixing 2-D TiO_2 catalyst (2.0 mg) with ABDA (5.0 mL) solution was saturated with oxygen for around 1 min followed by sealing with parafilm. A continuous wave (CW) laser was used as the light source. Under stirring, the above solution was irradiated with CW laser 532 nm and 750 nm. Absorbance of the solution at 377 nm was recorded using a UV-vis spectrometer. For comparison, the control experiment without 2-D TiO_2 catalyst was also performed with the same precedure.

5. Scanning tunneling microscopy (STM) measurement. STM experiments were carried out in an ultrahigh vacuum chamber of Unisoku LT-STM system with the base pressure (lower than 5.0×10^{-10} mbar). The polycrystalline tungsten wires were electrochemically etched to STM tips. The STM images were recorded at 77 K. Before measurement, the 2-D TiO_2 sample was dispersed in isopropanol and then loaded onto a Au (111) surface for atomic resolution STM image measurement. After annealing at 200 ˚C for 2 hours, the atomic resolution STM image was characterized with the applied bias voltage (V_{sample} = +340 mV). We used graphite as substrate for the thickness characterization of 2-D TiO_2 sheet. All STM experiments were performed at room temperature. WSxM software was used for the STM image data processing and analysis.

6. Characterizations. Transmission electron microscopy (TEM) and high-resolution transmission electron Microscopy (HR-TEM) were carried out using JEOL JEM-2100F TEM/STEM. The X-Ray Diffraction (XRD) pattern was recorded on Bruker D8 High-Resolution XRD featuring a four-bounce Ge (022) incident beam monochromator and highly monochromatic X-rays with Cu radiation (Cu Kα = 0.15406 nm). X-Ray photoelectron spectroscopy (XPS) measurements were conducted using a UHV vacuum generator VG ESCALAB 220I-XL system with a monochromatic Mg-Kα source. Before XPS measurement, the as-prepared sample was treated at 200 ^{o}C for 4 hours in oven to remove any adsorbed species. All the binding energies were referenced to the C1s peak at 284.6 eV of the surface adventitious carbon. The Raman data was collected on the Thermo Scientific DXR Raman microscope system and Renishaw Invia system with laser excitation of 532 nm and 780 nm, respectively. The UV-vis absorbance data was

obtained on a Shimadzu UV-2600 UV-visible spectrometer. We conducted the X-ray absorbance spectroscopic (XAS) investigation at Singapore Synchrotron Light Source.

7. Density functional theory (DFT) calculations. First principles calculations were performed with the plane-wave code VASP,[1] using projected augmented wave (PAW) potentials with the local density approximation (LDA)[2] to the exchange-correlation functional. The PAW potential of Ti has 12 electrons in valence ($3s^2$, $3p^6$, $3d^2$, $4s^2$). The monolayer is simulated by adding a vacuum thickness of 20 Å of vacuum to prevent interactions between periodic image slabs. An energy cut-off of 500 eV is used for the plane wave basis set. Increasing the cutoff energy to 550 eV gives similar results. The structures are considered as relaxed when the maximum component of the Hellmann−Feynman force acting on each ion is less than 0.01 $eV \cdot Å^{-1}$. The phonon band structure was computed using a 4×5×1 supercell,[3] where atoms are displaced to get the force constants that can build the dynamical matrix. The Raman frequencies and intensities of zone centre (Gamma point) phonons are calculated within density functional perturbation theory (DFPT)[4] as implemented in the Quantum Espresso Package.[5] The DFT simulated Raman spectra of anatase and lepidocrocite phase is obtained with an artifical Lorentzian broadening based on the calculated non-resonant Raman intensity. GW calculations are performed using the one-shot (G_0W_0) approach.[6-8] 288 bands (where 24 bands are occupied) are used in the GW calculation (decreasing this number to 240 changed the quasiparticle gap by only 0.02 eV). Using these GW energies, the Bethe-Salpeter equation (BSE)[9-10] (including the effect of electron-hole interaction) is solved to obtain the optical absorption spectra (288 bands were used in this calculation as well). Monkhorst-Pack k-point meshes of 9×11×1 and 9×13×1 are used to sample the

Brillouin Zones for the unstrained and stained TiO_2 monolayers. The calculated GW gaps are converged with respect to these k-point meshes (Table S4), and the major peak positions of the optical absorption spectra do not change significantly with the different k-point meshes used (Figure S13).

8. Elemental analysis. The chemical analysis (CHNS) and inductively coupled plasma-optical emission spectrometry (ICP) were carried out to provide information on the chemical composition and the Ti/O ratio of 2-D TiO_2 sheet. The commercial TiO_2 (P25) was employed to serve as the reference. Table S1 shows that both P25 and 2-D TiO_2 materials contain C and H, which may be related to the adsorbed C-containing species and H_2O. In addition, the 2-D TiO_2 material has a trace amount of S element (< 0.34 mol%), which is attributable to the surface adsorbed residues of S-containing molecules. The Ti/O ratio is confirmed to be about 1:2.

To further rule out S and N doping in the lattice of TiO_2, we performed detailed elemental analysis. A series of elemental analysis studies were carried out to test the contents of S in the as-prepared fresh sample after washing for different number of times. As shown in Table S2, we found that the C, H, N, and S elements could be gradually removed as we increased the number of times the sample was washed, from 3 to 10 times. These results suggest that C, H, N, and S stem from the remaining residuals adsorbed on the surface of 2-D TiO_2 sheets, and are not dopants in the lattice of TiO_2.

9. XPS and EDX analysis. We first made a comparison of the survey XPS data of the as-prepared 2-D TiO_2 sample after washing 3 times and after washing 10 times, as shown in Figure S1. Although weak signals of S and N were present after washing the sample 3 times, both of these two elements were only barely detectable after washing 10 times.

To elucidate the chemical states of S and N, we performed high-resolution XPS. The XPS S2p spectrum is characterized by a $S2p_{3/2}$ and $2p_{1/2}$ doublet with an energy separation of 1.2 eV. Figure S2 presents four different binding energies of $2p_{3/2}$ peaks in the range of 163-170 eV. According to the literature, these XPS S 2p peaks are likely to come from remaining surface residuals: C-S-C/C-S-S-C (at 163.4 eV) as a result of the addition of various reactive intermediates, including free radicals such as HS• and S•,[11-14] S or S-S (at 165.0 eV),[13, 15, 16] surface adsorbed SO_2 on TiO_2,(at 166.6 eV)[17, 18] and sulfate species (at 168.4 eV) formed by the sulfur oxidation in air.[11, 12] In the lower binding energy region (< 162.0 eV), we did not observe any S peak intensities in the TiO_2 sample after washing 3 times. This strongly suggests that there are no substitutional S dopants in the lattice of TiO_2, since Ti-S bonding would result in a binding energy of ~ 161.6 eV.[17, 19]

After washing 10 times, the S signal becomes very weak, as indicated in Figure S2b. Furthermore, the binding energy is located at ~166.7 eV, which is ascribed to surface adsorbed SO_2 on TiO_2 based on the literature.[17, 18] Such S species was not removed completely, probably due to the chemisorbed molecular SO_2 on the surface of TiO_2 in the form of Ti-O-S. This can explain the trace content of S (< 0.50 wt%) in the TiO_2 sample after washing 10 times, based on the elemental analysis (see Table S2) and EDX result (see Figure S3).

High resolution XPS also showed that after washing 3 times, a weak signal for the N 1s peak is observed, with a binding energy of ~ 401.4 eV (Figure S4a). According to the literature, this is likely to be due to C-N-H species in remaining organic residues, such as amino functional groups.[20-21] However, such N species were removed after washing 10

times and could not be detected in the high-resolution XPS N 1s spectrum (see Figure S4b). Furthermore, the N element was not found in EDX result in Figure S3.

Taken together, we conclude that the presence of S and N originate from remaining surface residuals, and are not lattice doped in TiO_2.

Table S1. Elemental analysis results of 2-D TiO_2 sheets and commercial P25.

Samples	Contents of Elements					
	Ti	**O**	**C**	**H**	**N**	**S**
P 25 (wt%)	61.08	37.70	< 0.50	0.72	/	/
P 25 (mol%)	28.92	53.73	0.95	16.39	/	/
2-D TiO_2 (wt%)	56.90	40.84	0.51	0.86	/	<0.50
2-D TiO_2 (mol%)	25.39	54.40	0.89	18.30	/	<0.34

Table S2. Elemental analysis of the as-prepared 2-D TiO_2 sample obtained after washing different times (3, 4, 5, 10).

washing times	Contents of Elements (wt%)					
	Ti	**O**	**C**	**H**	**N**	**S**
3	38.60	32.46	16.77	3.72	2.38	6.07
4	41.56	32.32	15.50	3.29	2.8	4.53
5	39.47	42.12	13.72	2.61	< 0.50	1.58
10	56.90	40.34	0.51	0.86	/	< 0.50

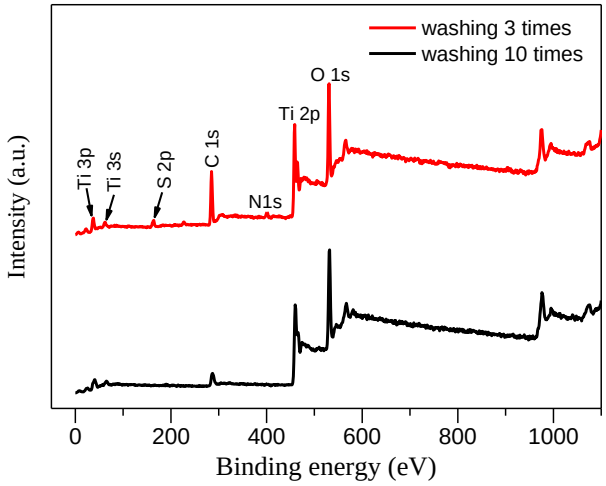

Figure S1. Comparison of survey XPS spectra of 2-D TiO_2 sample after washing 3 times, and after washing 10 times.

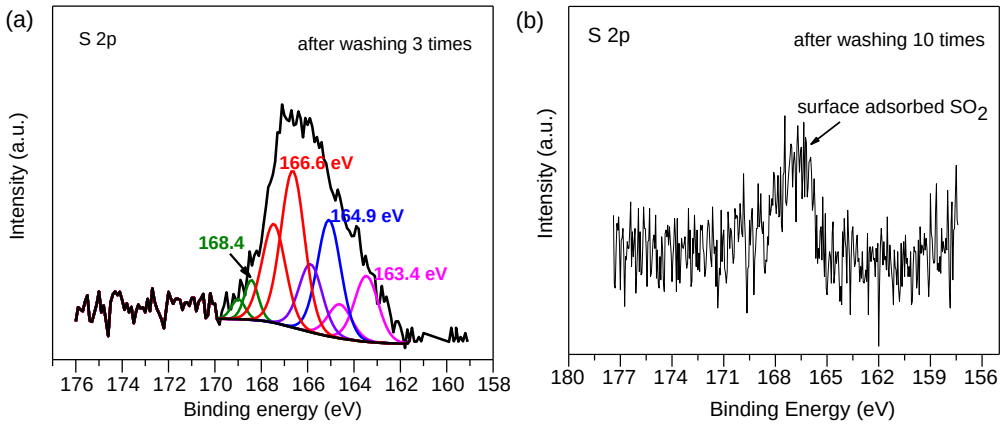

Figure S2. Comparison of high-resolution XPS S 2p spectra (a) and (b) of the 2-D TiO_2 sample after washing 3 and 10 times, respectively.

No peaks omitted

Element	Weight %	Atomic%
C K	39.71	65.08
O K	15.48	19.05
Si K	0.36	0.25
S K	0.32	0.20
Ti K	17.32	7.12
Cu K	26.81	8.31
Total	100.0	

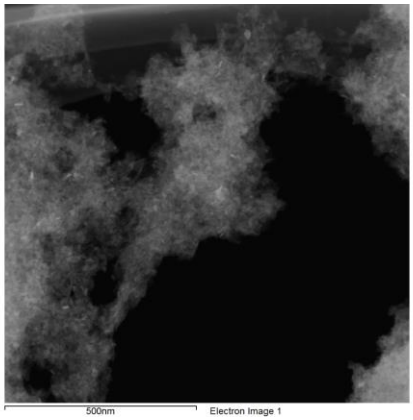

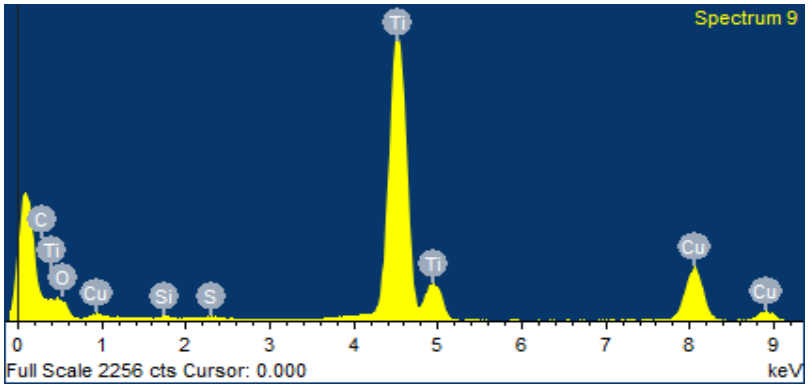

Figure S3. EDX result of the synthesized 2-D TiO_2 sample after washing 10 times.

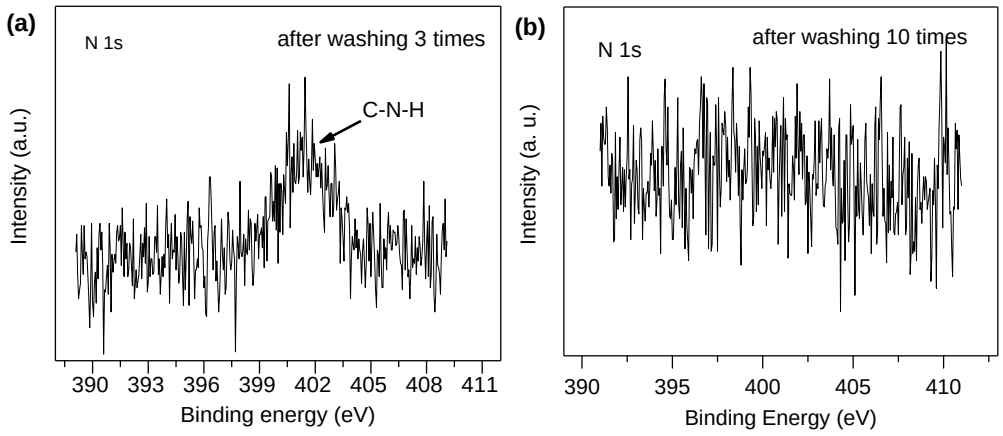

Figure S4. Comparison of high-resolution XPS N 1s spectra (a) and (b) of the 2-D TiO_2 sample after washing 3 and 10 times, respectively.

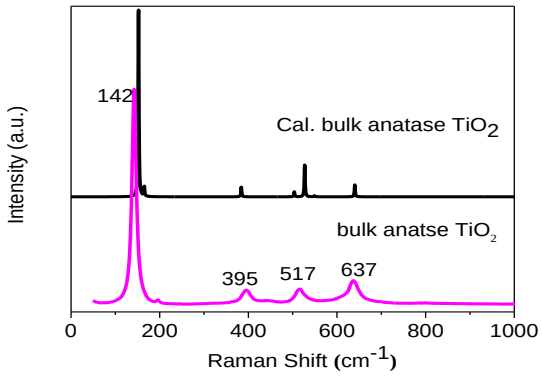

Figure S5. Calculated (black) and experimental (purple) Raman spectra of bulk anatase TiO_2.

Table S3. Comparison between the calculated Gamma point phonon frequencies of lepidocrocite TiO_2 monolayer and the experimental Raman peak frequencies of the 2-D TiO_2. The irreducible representation (Irr.), computed normalized Raman intensity and optical activity are also given.

DFT-Calculations					Experiment
mode	frequency (cm^{-1})	Irr.	Raman intensity	optical activity	frequency (cm^{-1})
1	0	B_u	0	I	
2	0	A_u	0	I	
3	0	B_u	0	I	
4	113.01	B_g	0.02	R	111
5	177.89	B_g	0.02	R	185
6	235.49	B_u	0	I	
7	238.27	B_u	0	I	
8	249.66	B_g	0.05	R	266
9	278.62	A_g	0.62	R	282
10	384.5	B_g	0.02	R	383
11	450.02	A_g	0.58	R	444
12	462.77	B_u	0	I	
13	525.5	B_u	0	I	
14	540.93	B_g	0.02	R	
15	579.8	A_u	0	I	
16	683.76	B_g	0.03	R	669
17	718.38	A_g	1.00	R	700
18	726.16	A_u	0	I	

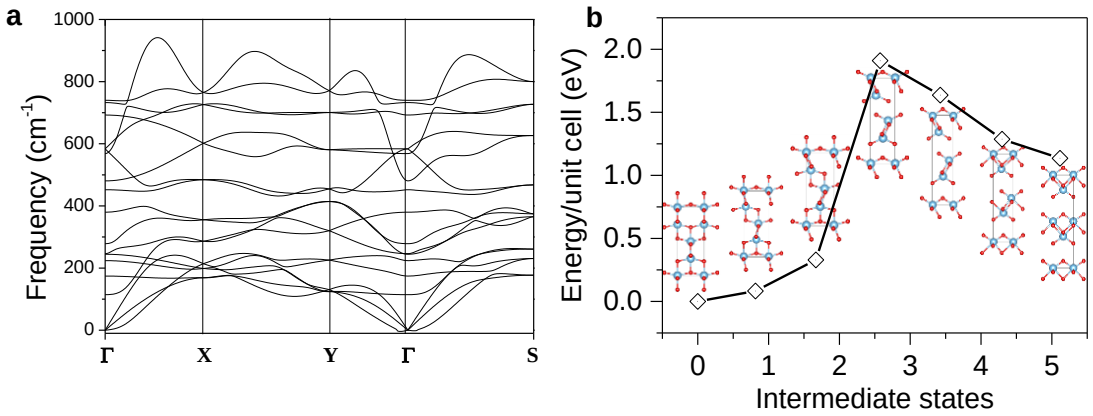

Figure S6. (a) Phonon dispersion of monolayer lepidocrocite phase TiO_2; (b) The energies of possible intermediate states from the anatase phase to the lepidocrocite phase; the energy of the anatase phase is set as the reference. We note that this calculation gives only an estimate to the energy barrier for transition, due to difficulty in converging the nudged elastic band calculation.

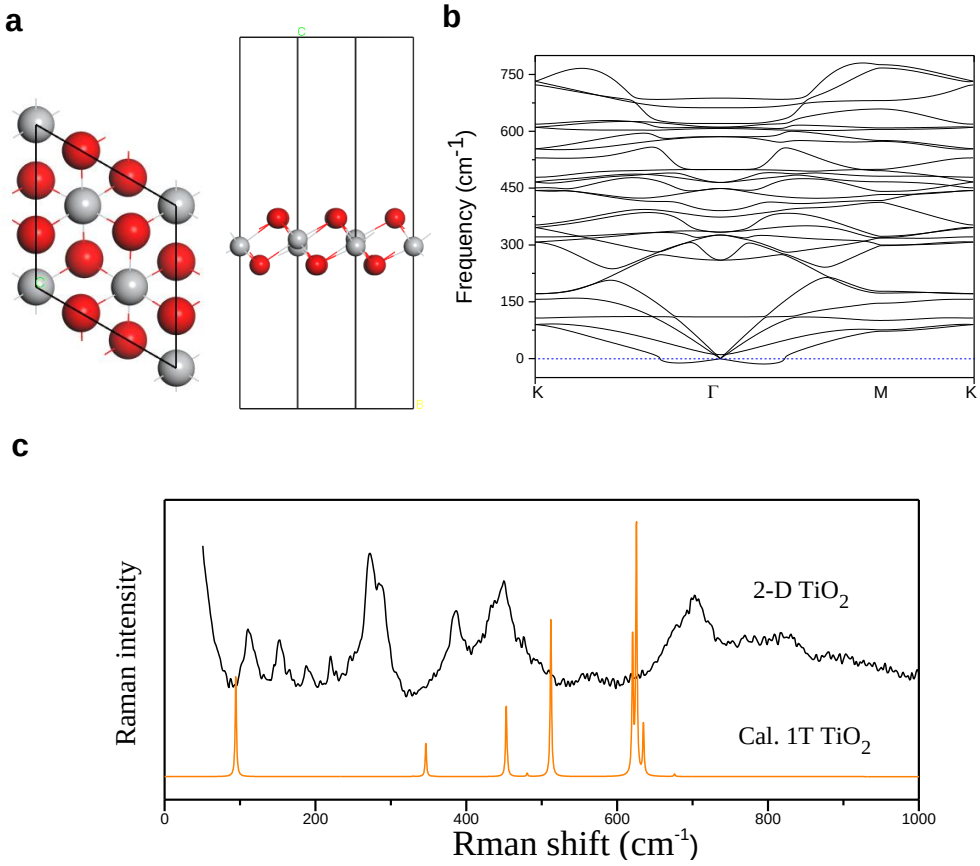

Figure S7. 2-D T phase TiO_2 constructed based on the STM atomic images. (a) Top view and side view of the structure. (b) the phonon dispersion of T phase TiO_2, the imaginary frequences (denoted as negative frequencies) indicate that the structure is unstable. This is consistent with other reports of the perfect hexagonal T phase exhibiting distortions that require larger unit cells. (c) The simulated Raman spectrum of the 1T phase single-layer TiO_2 does not match well with the experimental data.

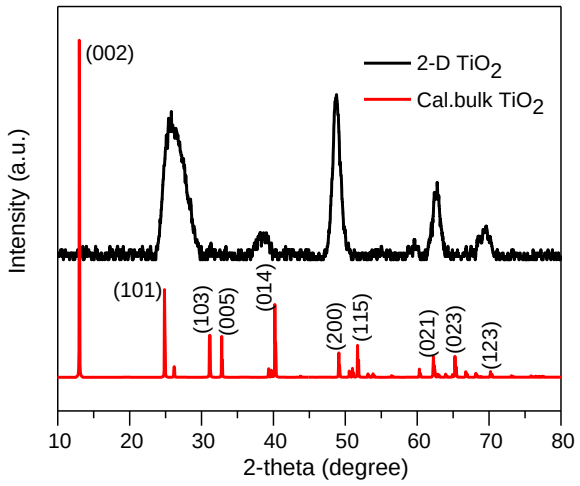

Figure S8. Comparison of the peak positions in the experimental XRD pattern and those simulated for bulk lepidocrocite TiO_2. The peak positions in these two XRD patterns match reasonably well, except for the peaks that correpond to the out-of-plane (002) and (005) diffraction direction of the bulk; it is missing in the 2-D sample as we expect.

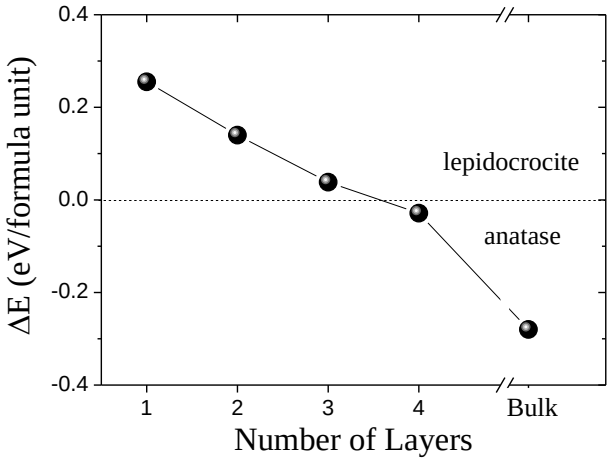

Figure S9. Energy difference between the anatase and lepidocrocite phase TiO_2 for thin films of different thickness and for the bulk. A positive energy difference indicates that the lepidocrocite phase is more stable, and a negative energy difference indicates that the anatase phase is more stable.

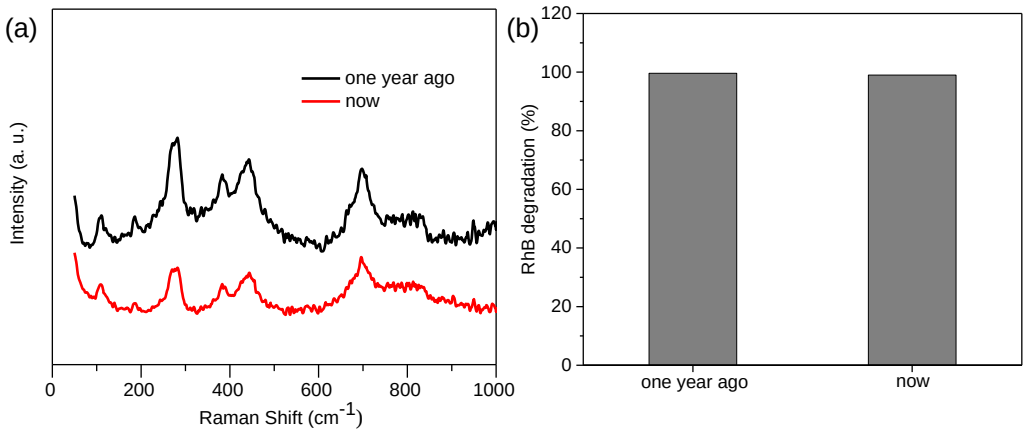

Figure S10. 2-D TiO_2 material synthesized one year ago: comparison of (a) Raman spectra and (b) photocatalytic RhB degradation under visible light irradiation ($\lambda \geq 420$ nm).

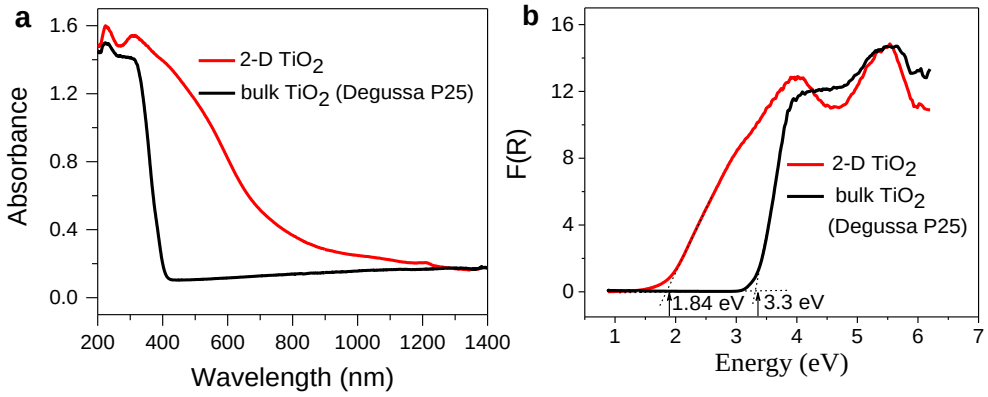

Figure S11. (a) UV-Vis absorption spectra of as-prepared 2-D TiO_2 and bulk TiO_2 (Degussa P25) in the range of 200-1400 nm. (b) Kubelka-Munk Plots transformed from the reflectance. The optical band gaps were estimated by extending the slopes of the curve, to intercept with the energy axis.

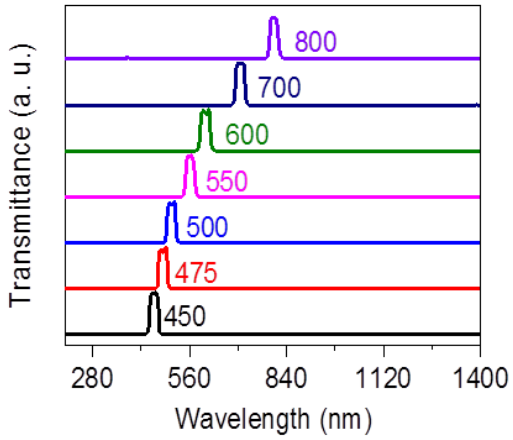

Figure S12. The optical spectra of the filters used for the photocatalytic measurements, such as the photocurrent densities and the degradation of MB. These band-pass light filters, 450, 475, 500, 550, 600, 700, and 800 nm were fixed on the light source Xenon lamp (500 W) simulating sunlight.

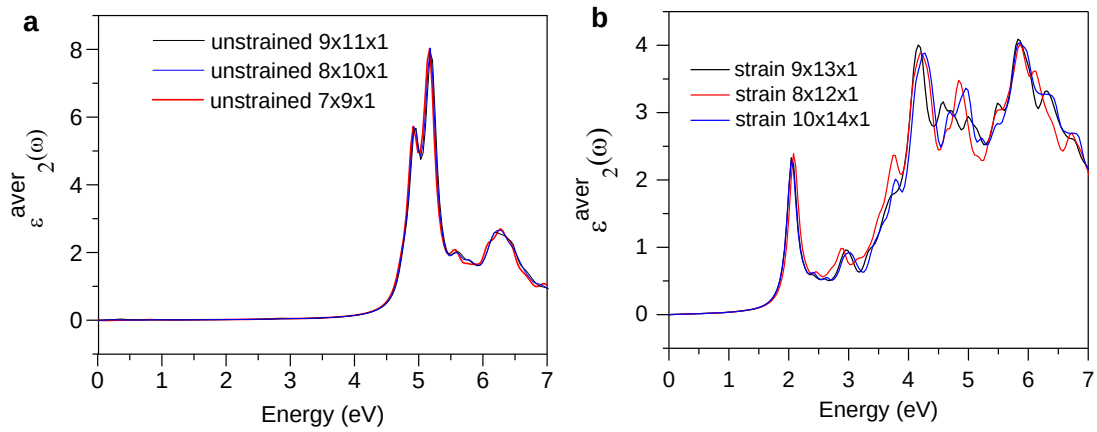

Figure S13. Convergence test with respect to the density of the Monkhorst-Pack k-point mesh, for the imaginary part of the dielectric constants of the unstrained and strained one-layer lepidocrocite TiO_2.

Table S4. Convergence test with respect to the density of the Monkhorst-Pack k-point mesh, for the GW gap of unstrained and strained TiO_2 monolayers.

	Unstrained TiO_2				Strained TiO_2			
	LDA	GW			LDA	GW		
k-point mesh	8x10x1	7x9x1	8x10x1	9x11x1	9x13x1	8x12x1	9x13x1	10x14x1
VBM (eV)	-5.75	-6.06	-6.04	-6.02	-3.92	-4.17	-4.01	-4.02
CBM (eV)	-2.66	-0.02	-0.04	-0.05	-2.96	-1.20	-1.13	-1.16
GW gap (eV)	3.09	6.04	6.00	5.97	0.96	2.98	2.88	2.86

References

1. Kresse, G.; Hafner, J. *Phys. Rev. B* **1993,** *47*, 558.
2. Perdew, J. P.; Zunger, A. *Phys. Rev. B* **1981,** *23*, 5048-5079.
3. Togo, A.; Tanaka, I. *Scr. Mater.* **2015,** *108*, 1-5.
4. Lazzeri, M.; Mauri, F. *Phys. Rev. Lett.* **2003,** *90*, 036401.
5. Paolo, G.; Stefano, B.; Nicola, B.; Matteo, C.; Roberto, C.; Carlo, C.; Davide, C.; Guido, L. C.; Matteo, C.; Ismaila, D.; Andrea Dal, C.; Stefano de, G.; Stefano, F.; Guido, F.; Ralph, G.; Uwe, G.; Christos, G.; Anton, K.; Michele, L.; Layla, M.-S.; Nicola, M.; Francesco, M.; Riccardo, M.; Stefano, P.; Alfredo, P.; Lorenzo, P.; Carlo, S.; Sandro, S.; Gabriele, S.; Ari, P. S.; Alexander, S.; Paolo, U.; Renata, M. W. *J.Phys. Condens. Matter* **2009,** *21*, 395502.
6. Hybertsen, M. S.; Louie, S. G. *Phys. Rev. B* **1986,** *34*, 5390-5413.
7. Shishkin, M.; Kresse, G. *Phys. Rev. B* **2006,** *74*, 035101.
8. Shishkin, M.; Kresse, G. *Phys. Rev. B* **2007,** *75*, 235102.
9. Albrecht, S.; Reining, L.; Del Sole, R.; Onida, G. *Phys. Rev. Lett.* **1998,** *80*, 4510-4513.
10. Rohlfing, M.; Louie, S. G. *Phys. Rev. Lett.* **1998,** *81*, 2312-2315.
11. Li, G.; Sun, J.; Hou, W.; Jiang, S.; Huang, Y.; Geng, J. *Nat. Commun.* **2016,** *7*, 10601.
12. Wang, Z.; Dong, Y.; Li, H.; Zhao, Z.; Wu, H. B.; Hao, C.; Liu, S.; Qiu, J.; Lou, X. W. D. *Nat. Commun.* **2014,** *5*, 5002.

13. Liu, C.; Han, R.; Ji, H.; Sun, T.; Zhao, J.; Chen, N.; Chen, J.; Guo, X.; Hou, W.; Ding, W. *Phys. Chem. Chem. Phys.* **2016,** *18*, 801-810.
14. Steudel, R. *Ind. Eng. Chem. Res.* **1996,** *35*, 1417-1423.
15. Gao, H.; Liu, Z.; Song, L.; Guo, W.; Gao, W.; Ci, L.; Rao, A.; Quan, W.; Vajtai, R.; Ajayan, P. M. *Nanotechnology* **2012,** *23*, 275605.
16. Paraknowitsch, J. P.; Wienert, B.; Zhang, Y.; Thomas, A. *Chem-Eur. J.* **2012,** *18*, 15416-15423.
17. Umebayashi, T.; Yamaki, T.; Yamamoto, S.; Miyashita, A.; Tanaka, S.; Sumita, T.; Asai, K. *J. Appl. Phys.* **2003,** *93*, 5156-5160.
18. Tang, X.; Li, D. *J. Phys. Chem. C* **2008,** *112*, 5405-5409.
19. Lin, T.; Yang, C.; Wang, Z.; Yin, H.; Lü, X.; Huang, F.; Lin, J.; Xie, X.; Jiang, M. *Energ. Environ. Sci.* **2014,** *7*, 967-972.
20. Xiao, J.; Xie, Y.; Nawaz, F.; Jin, S.; Duan, F.; Li, M.; Cao, H. *Appl. Catal. B: Environ.* **2016,** *181*, 420-428.
21. Wang, R.-C.; Yin, T.-L.; Wei, P.-J.; Liu, J.-G. *RSC Adv.* **2015,** *5*, 66487-66493.